Global-mean marine $\delta^{13}C$ and its uncertainty in a glacial state estimate

Geoffrey Gebbie[a], Carlye D. Peterson[b], Lorraine E. Lisiecki[b], Howard J. Spero[c]

[a]*Department of Physical Oceanography, Woods Hole Oceanographic Institution, 360 Woods Hole Rd., MS # 29, Woods Hole, MA, 02543 USA, ggebbie@whoi.edu*
[b]*Department of Earth Science, University of California, Santa Barbara, California, USA*
[c]*Department of Earth and Planetary Sciences, University of California, Davis, California, USA*

Abstract

A recent paleo-data compilation with over 450 $\delta^{13}C$ and $\delta^{18}O$ observations provides the opportunity to sample the Last Glacial Maximum (LGM) well enough to infer its global properties, such as the mean $\delta^{13}C$ of dissolved inorganic carbon. Here, the paleo-compilation is used to reconstruct a steady-state circulation field for the LGM, that in turn is used to map the data onto a 3D global grid. A global-mean marine $\delta^{13}C$ value and a self-consistent uncertainty estimate are derived using the framework of state estimation (i.e., inverse methods). The LGM global-mean $\delta^{13}C$ is estimated to be $0.14‰ \pm 0.20‰$ at the two standard error level, giving a glacial-to-modern change of $0.32‰ \pm 0.20‰$. The magnitude of the error bar is attributed to the uncertain glacial ocean circulation and the lack of observational constraints in the surface Pacific and Southern Oceans. A manipulated circulation field can even yield a mean $\delta^{13}C$ change of $0.6‰$, in basic consistency with inferences of terrestrial carbon reservoir change.

Keywords: Paleoceanography, Physical Oceanography, Carbon reservoirs, Last Glacial Maximum, Inverse methods

1. Introduction

Carbon-13 to carbon-12 ratios (i.e., $\delta^{13}C$) can chemically fingerprint different carbon reservoirs, and thus the global-mean glacial-interglacial change in $\delta^{13}C$ of oceanic dissolved inorganic carbon (i.e., $\delta^{13}C_{DIC}$) reflects the carbon partitioning between terrestrial, atmospheric, and marine reservoirs. Dramatic environmental changes during the Last Glacial Maximum (LGM, 19-23 ka) altered the terrestrial biosphere, and some of the low isotopic signature of terrestrial carbon ($\delta^{13}C \approx -25‰$) was transferred to the glacial ocean, consistent with observations of benthic foraminiferal $\delta^{13}C$ lower than the modern-day (e.g., Shackleton, 1977; Curry et al., 1988; Duplessy et al., 1988). The glacial atmosphere held approximately 170 gigatons (Gt) less carbon, leaving the ocean as the most readily available source of compensation for the other two reservoirs. Pollen records and vegetation models that more directly reflect terrestrial carbon change yield higher estimates of glacial-to-modern carbon transfer (e.g., 750 to 1900 Gt C, Crowley, 1995; Adams and Faure, 1998; Kaplan et al., 2002) than the marine-based estimates (e.g., 330 to 650 Gt C, Shackleton, 1977; Curry et al., 1988; Duplessy et al., 1988; Köhler et al., 2010). A recent compilation of benthic *Cibicidoides* spp. $\delta^{13}C$ has nearly twice the data points of previous compilations and coverage of the Atlantic, Pacific, and Indian Oceans (Peterson et al., 2014), and thus motivates the re-investigation of the marine-based whole-ocean $\delta^{13}C$ estimates.

Determining the mean value of a spatially-distributed tracer field boils down to a linear operation in most cases (i.e., an inner vector product):

$$\overline{c} = \sum_{i=1}^{N} w_i y_i + \overline{c}_0 = \mathbf{w}^T \mathbf{y} + \overline{c}_0 \tag{1}$$

where $\overline{c}$ is the global mean value, $\mathbf{w}$ is a vector of weights with w_i for the ith el-

ement, T is the vector transpose, $\mathbf{y}$ is a vector containing N observations, and $\overline{c}_0$ is a constant included for full generality. If all observations are assumed to contain equal information about the global mean and no prior information is available ($\overline{c}_0 = 0$), the optimal weights would all be $1/N$, and equation (1) reverts to the basic sample mean. The sparse, irregularly-spaced nature of glacial observations invalidates this assumption, of course. Originally, paleoceanographers best dealt with this issue by choosing cores from what was thought to be the most representative oceanic regions (e.g., Shackleton, 1977). As more data became available, basin-wide or regional means were computed as a preliminary step before global averaging (e.g. Curry et al., 1988; Boyle, 1992; Matsumoto and Lynch-Stieglitz, 1999; Peterson et al., 2014). This multi-step process naturally leads to non-uniform weights on the observations in equation (1).

The global mean computed as a succession of sub-averages may be sensitive to the size and location of the sub-domains, and only by producing δ^{13}C maps at higher spatial resolution will this sensitivity disappear. The distance between LGM observations, however, is often greater than the decorrelation lengthscale of oceanic property fields, and thus the typical method of "objectively" mapping the observations onto a regular grid (e.g., optimal interpolation or objective mapping, Bretherton et al., 1976) will revert to a first-guess estimate in many locations. In other words, large regions of the LGM ocean would be unconstrained by the data, especially at intermediate depths where little core coverage is available. Furthermore, the objectively-mapped estimate will leave local extrema in the estimated tracer field around the data points. Such features are undesirable because they are not physically sustainable in equilibrium when diffusion has sufficient time to act (e.g., in the case of atmospheric momentum, Hide, 1969), although it is not

clear how equilibrated the glacial ocean was. For a nonconservative tracer such as $\delta^{13}C_{DIC}$, local minima (but not maxima) may exist in conjunction with an interior tracer sink due to remineralization. A new method is needed to create a map with such sparse observations while addressing these complications.

Here we suggest that a method originally developed for estimating the ocean circulation from sparse observations (Gebbie, 2014) is also well-suited to make three-dimensional global maps. Specifically, we combine observations with a numerical model to produce an LGM state estimate. Additionally, we outline a method to determine the observational weights, $\mathbf{w}$, that takes sampling characteristics and ocean circulation into account. Rather than using the assumed statistics of circulation lengthscales, we suggest that the circulation itself can be used to make a better gridded field. The numerical model serves a dual purpose: 1) a means to readily interpret the sources, sinks, and pathways of tracer, and 2) a kinematic interpolator and extrapolator that allows large-scale information to be extracted from the observations.

This work is divided into two major parts: 1) estimating the LGM global-mean $\delta^{13}C_{DIC}$, and 2) diagnosing and understanding its uncertainty. The first part introduces the numerical model, observations, and the 3D mapping technique (Section 2). This technique allows the reconstruction of a global map of LGM $\delta^{13}C_{DIC}$ and the emergence of a coherent pattern of LGM-to-modern changes (Section 3). The second part extends the state estimation framework to produce uncertainty estimates with the attribution of the sources of uncertainty (Section 4). An uncertainty estimate is produced for glacial-mean $\delta^{13}C_{DIC}$, as well as regional estimates (Section 5). Then we interpret the sources of the uncertainty and put it into the context of previous works (Section 6), before concluding (Section 7).

2. Global LGM state estimate

The global LGM state estimate is produced by combining a kinematic ocean circulation model with a global array of benthic foraminiferal observations of $\delta^{13}C$ and $\delta^{18}O$. The model and observations are detailed next.

2.1. Model

Multiple tracers are modeled for the glacial ocean simultaneously: potential temperature, salinity, seawater $\delta^{18}O$, phosphate, and $\delta^{13}C_{DIC}$. The model is a statistically steady-state conservation equation that is assumed to hold for, c, a general tracer: $\nabla \cdot (\vec{f} c) = q$, where $\vec{f}$ is the mass flux and q is a local source or sink. In the statistical steady state, any temporal variability that has a net diffusive or advective effect can be represented by the model used here. For the isotope variables, an error is incurred by modeling the ratio rather than the individual isotopes (e.g., Walker, 1991), but this error is damped in the vicinity of observations by the formal data constraints. In particular, the sink of $\delta^{13}C_{DIC}$ due to remineralization is assumed to be equal to -0.95 times the source of remineralized phosphate, which is adjusted relative to the modern ratio of -1.1 due to changes in whole-ocean $\delta^{13}C_{DIC}$ and upper-ocean biological fractionation (e.g., following Broecker and Maier-Reimer, 1992). For conservative tracers, the source and sink vanishes ($q = 0$). A global grid is defined with $4^\circ \times 4^\circ$ horizontal resolution and 33 vertical levels with enhanced resolution near the surface.

2.2. Observations

A major extension to the work of Gebbie (2014) is the use of the paleo-data compilation of Peterson et al. (2014) that includes observations in the Pacific and

Indian sectors, rather than the Atlantic-only data used previously. This compilation contains 376 $\delta^{13}C$ and 369 $\delta^{18}O$ measurements from benthic foraminifera dated to the Last Glacial Maximum from 19,000 to 23,000 years before present (19-23 kyr BP) following a re-derived age model (Stern and Lisiecki, 2014). The need for inter-species and interlaboratory offsets is reduced by compiling only *Cibicidoides* spp. $\delta^{13}C$ data, and by implementing $\delta^{18}O$ constraints based on the LGM-to-Late Holocene difference in the same core. Other data are added (e.g., personal communication, D.W. Oppo and W. Curry, Marchal and Curry, 2008; Makou et al., 2010; Hesse et al., 2011), including porewater salinity and $\delta^{18}O$ data points (Adkins et al., 2002). The deglacial records indicate a group of outliers where the LGM-to-Holocene $\delta^{18}O$ change is less than 0.6‰, which can be traced back to low temporal resolution in the cores. Therefore we have removed these values from the compilation. Observations were also culled when the phytodetritus effect was implicated by the original authors (e.g., Mackensen et al., 2000), and at locations that fall more than 200km outside of the model grid. In total, 492 LGM $\delta^{13}C$ and $\delta^{18}O$ data points constrain the model simulation (locations are later shown in Figure 7).

2.3. Solution method

Our solution method must fit the model to the observations and also handle nonlinearities, including gravitational stability, the non-negativity of tracer concentrations, and the multiplication of uncertain tracer concentrations with uncertain circulation fields. The nonlinear optimization problem is solved via a hand coding of the adjoint equation that describes the evolution of the Lagrange multipliers (see supporting information of Gebbie (2014)), and is solved iteratively using a limited-memory quasi-Newton gradient descent routine (Nocedal, 1980).

The resulting $\delta^{13}C_{DIC}$ distribution fits the observations with a standard deviation of the misfit of 0.19‰ that is an acceptable fit within the expected uncertainty of 0.2‰ in the data. This expected value is based upon the proxy error calculated by the Late Holocene core data to modern-day seawater data misfits. 50% of the points are fit within 0.02‰, although outliers larger than ±0.6‰ exist. While not being the primary variable of interest here, $\delta^{18}O$ is also fit well, with a standard deviation of 0.22‰ that is approximately equal to the expected value of 0.2‰.

We are motivated by the atmospheric pCO_2 change of 80-100ppm from the LGM to the pre-industrial era, and thus we seek to estimate the marine $\delta^{13}C$ change over the same time period, here denoted $\Delta_{MG}[\delta^{13}C_{DIC}]$ (i.e., modern, "M," minus glacial, "G"). A modern-day reference circulation that attempts to reconstruct the pre-industrial ocean was produced using the same method (Gebbie, 2014) and will be used for comparison here. The GLODAP and CARINA seawater $\delta^{13}C_{DIC}$ compilation (Schmittner et al., 2013) constrained the modern-day distribution, and observations in the upper 1km of the water column were downweighted in an attempt to account for the Suess effect (e.g., Olsen et al., 2006) and to produce a pre-industrial gridded $\delta^{13}C_{DIC}$ distribution. Note that most marine estimates were based on glacial-to-Late Holocene differences (here distinguished by the notation, $\Delta_{HG}[\delta^{13}C_{DIC}]$) that may reflect a different quantity due to the core information ending asynchronously over the last few thousand years of the Holocene. Modern-day and glacial ocean computations are undertaken on the same grid, but gridcells above 120 meters modern-day water depth are discarded in the glacial case.

3. Glacial-mean $\delta^{13}C$

The global mean of any LGM tracer is calculated as the mass-weighted average of the tracer concentration in each gridcell. As three-dimensional fields are modeled for temperature and salinity, the mass of each gridcell is determined by the product of the cell volume and the seawater density as calculated by the international thermodynamic equation of state (IOC, 2010). Although the LGM density field is not well constrained, the spatial range of density has variations no larger than 5%, and thus volume (set by the size of the gridcells) dominates the calculation. The glacial global mean $\delta^{13}C$ is estimated to be 0.14‰, leading to an estimate of glacial-to-modern change of 0.32‰ when comparing to the reference (modern) state estimate. This estimate results from a spatially structured pattern of change, shown next.

3.1. LGM $\delta^{13}C$ distribution

The main characteristic of the LGM North Atlantic $\delta^{13}C$ distribution is a depletion of $\delta^{13}C_{DIC}$ below 2km depth (upper panel, Figure 1) that conforms with expectations (e.g., Duplessy et al., 1988; Curry and Oppo, 2005). The $\delta^{13}C_{DIC}$ gradient with depth is not as sharp as in the inversion of Gebbie (2014), due to zonal averaging over the entire Atlantic basin, but also reflecting a spurious smearing effect in the large data compilation sourced from multiple laboratories. For the present focus of seeking global and regional means, weaker gradients are unimportant so long as the center of the high-gradient interface is at the right depth, as it appears to be. Of more concern are the undersampled regions, where this inversion sometimes disagrees with the Gebbie (2014) inversion. For example, the updated state estimate has a much higher $\delta^{13}C_{DIC}$ in the Arctic (1.2‰ compared to

0.6‰). The Southern Ocean endmember is -0.8‰ in both inversions, but should not necessarily be interpreted as a robust result. The uncertainty of the estimate in these regions without data will be explicitly addressed in the next section. In the Pacific, the most depleted LGM Pacific $\delta^{13}C_{DIC}$ values deepen from 1.5km in the modern-day to almost 3km (e.g., Matsumoto et al., 2002; Herguera et al., 2010), and our gridded field shows how this structure fits into the surface and Southern Ocean distribution (lower panel, Figure 1).

Besides the $\delta^{13}C$ distribution, we also solve for the circulation (actually, water-mass distribution) that is consistent with the seawater properties. The inferred LGM Atlantic circulation is similar to the previous inversion of Gebbie (2014), with an increased return flow of North Atlantic Water to bottom waters relative to intermediate waters. In addition, the 50% southern source isoline is around 4km depth in the North Atlantic (this is also the place where southern and northern source water concentrations are equal). Significant deep remineralization (with the addition of ^{12}C effectively causing a sink of $\delta^{13}C$) was originally reported in the deep Atlantic (Gebbie, 2014), but is less pronounced in the updated state estimate due to the use of a more spatially-coherent $\delta^{18}O$ dataset (derived from LGM-to-Late Holocene differences). The estimated LGM Pacific has deeper North Pacific Water (down to 2km instead of 800m today, as defined by the 50% concentration line). Otherwise southern water masses fill the same part of the Pacific sector.

3.2. Spatial pattern of $\delta^{13}C$ change

The difference of the modern-day and LGM gridded $\delta^{13}C_{DIC}$ fields permits the mapping of a global, three dimensional field of $\Delta_{MG}[\delta^{13}C_{DIC}]$, where large-scale coherent patterns emerge (Figure 2). In much of the Atlantic and Pacific Oceans

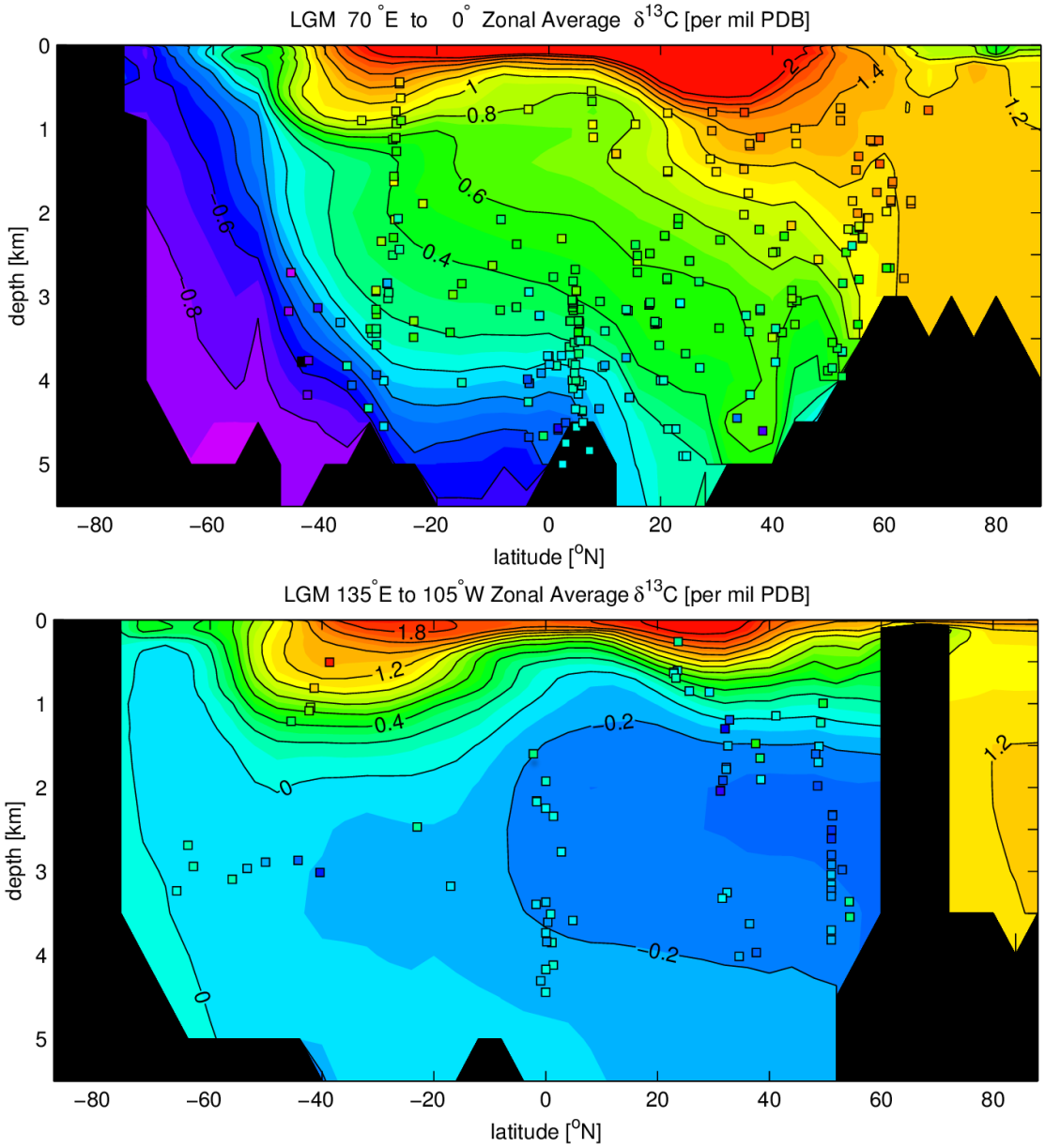

Figure 1: LGM Atlantic (*upper*) versus Pacific (*lower*) $\delta^{13}C_{DIC}$, with all observations from the particular basin (*colored squares*) and 3D gridded field (*background colors and contours*). All Atlantic sections are zonally averaged from 70°W to 0°, and all Pacific sections are zonally averaged from 135°E to 105°W. The colored symbols are on the same color scale as the background field.

above 1km, $\delta^{13}C_{DIC}$ decreased over the deglaciation despite the increase in the global mean. In general, $\Delta_{MG}[\delta^{13}C_{DIC}]$ increases with depth and toward the south in these two ocean basins, however, the biggest changes are reserved for the Atlantic sector of the Southern Ocean. While a previous study showed little $\delta^{13}C_{DIC}$ change above 2km in the North Pacific (Matsumoto et al., 2002), here we find that the North Pacific $\delta^{13}C$ drops over the deglaciation by more than 0.8‰ between 300 and 1100 meters depth. In intermediate waters, our map suggests a scenario closer to that described by Herguera et al. (2010), where the intermediate South Pacific $\delta^{13}C_{DIC}$ increases, but the intermediate North Pacific decreases. Overall, $\delta^{13}C_{DIC}$ actually decreases in many locations, and the global mean value results from the competing influence of regions with differing signs of change.

4. Uncertainty of the state estimate

4.1. Deriving an uncertainty formula

A major focus of this work is the determining the uncertainty of the global mean and attributing the sources of that uncertainty. The uncertainty, $\mathbf{P}_{\bar{c}}$, is defined as the expected squared difference between the estimated global mean, $\tilde{\bar{c}}$, and the true value, $\bar{c}$ (i.e., $\mathbf{P}_{\bar{c}} \equiv < (\tilde{\bar{c}} - \bar{c})^2 >$), where the brackets indicate the expected value operator (e.g., Wunsch, 1996). This matrix becomes a scalar when $\bar{c}$ is a scalar. As a complete uncertainty analysis of this large, nonlinear problem would require computational resources beyond our capacity, we instead derive the uncertainty with a local, linearized approach. For an unbiased estimator, the true solution, $\bar{c}$, may be set equal to the expected value that would emerge from our estimation method over many different realizations, $< \tilde{\bar{c}} >$, but here we restrain from such an interpretation given the highly nonlinear nature of the problem and the

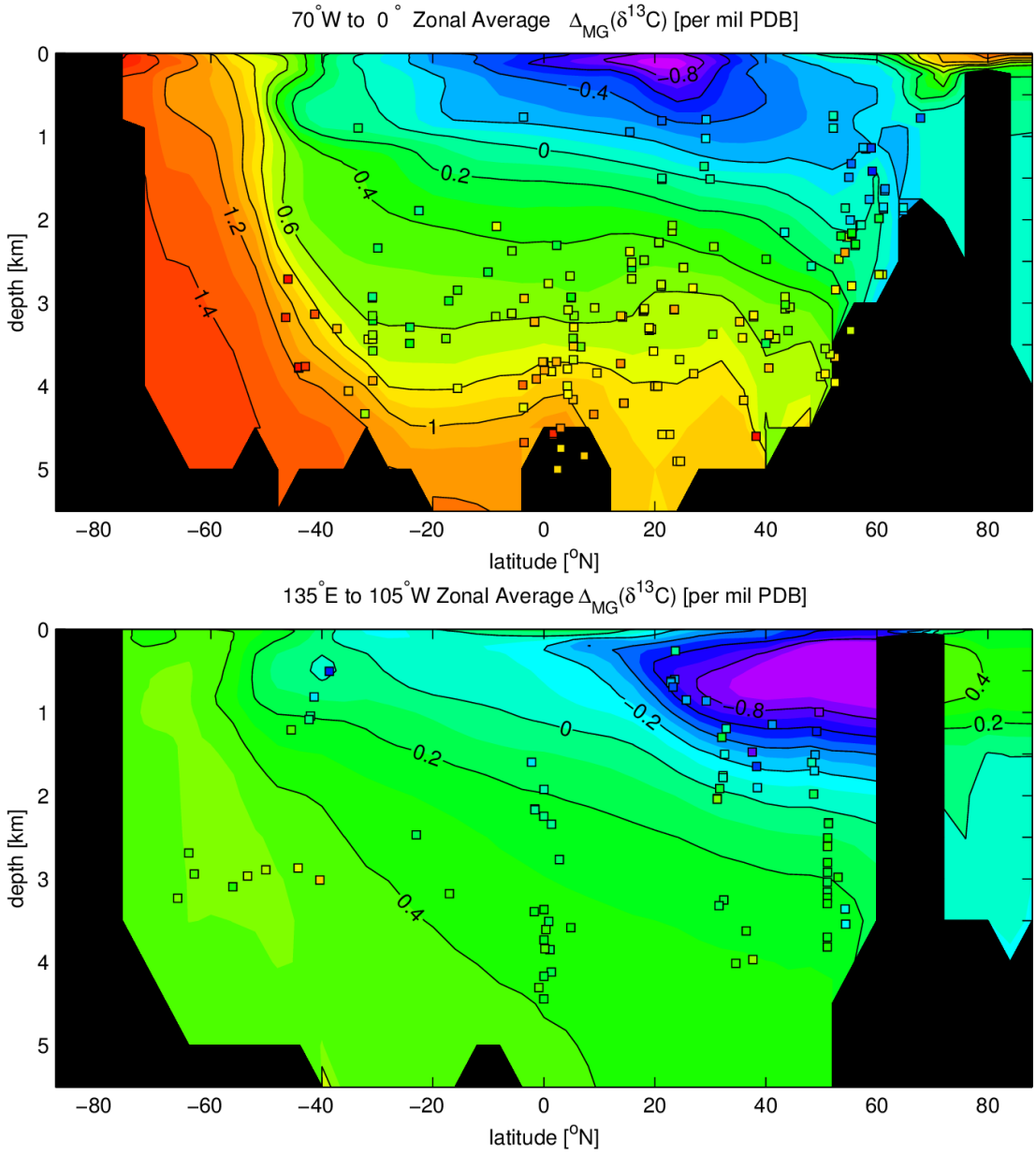

Figure 2: Similar to Figure 1, but for the Atlantic and Pacific zonal-average difference in $\delta^{13}C_{DIC}$ between the modern-day and LGM (i.e., $\Delta_{MG}[\delta^{13}C_{DIC}] = \delta^{13}C^{M}_{DIC}$ - $\delta^{13}C^{G}_{DIC}$).

simplified nature of the model. Thus we are restricted to solving for the expected range of solutions, here defined as the dispersion of $\tilde{\bar{c}} - <\tilde{\bar{c}}>$ or equivalently the solution covariance, $\mathbf{C}_{\bar{c}} \equiv <(\tilde{\bar{c}} - <\tilde{\bar{c}}>)^2>$. The standard error, $\sigma_{\bar{c}}$, is then defined as the square root of the solution covariance: $\sigma_{\bar{c}} \equiv \sqrt{\mathbf{C}_{\bar{c}}}$. Our estimate of the glacial-mean $\delta^{13}C_{DIC}$ uncertainty will later be quoted as twice the standard error.

To calculate the uncertainty of the global mean, we first define the global mean explicitly (following Section 3). For reasons that should become clear below, the state vector, $\mathbf{x}$, is defined to contain both tracer and circulation information, i.e., $\mathbf{x}^T = [\mathbf{c}; \mathbf{m}]^T$, where $\mathbf{c}$ is a vector that represents any global three-dimensional tracer distribution and $\mathbf{m}$ describes the circulation as a vector of mass-flux ratios between grid faces (e.g., Gebbie and Huybers, 2010). This state vector definition is not unique, but it provides sufficient information to permit a steady-state tracer distribution to be computed, and thus is an acceptable definition of the state. The mass-weighted global mean is operationally defined as $\bar{c} = \mathbf{r}^T \mathbf{x}$, where $\mathbf{r}$ is the appropriately-defined mass-weighting vector (i.e., $r_i = M_i / \sum_{j=1}^{J} M_j$ for all $i \leq J$, $r_i = 0$ for all $i \geq J$, M_i is the mass of gridcell i, and the global ocean has J gridcells). The sum of elements of $\mathbf{r}$ is equal to one to form a proper average ($||\mathbf{r}||_1 \equiv 1$).

Substituting the equation for the global mean into the definition of the global-mean covariance, the uncertainty of the global mean is clearly dependent upon the uncertainty over the entire globe:

$$\mathbf{C}_{\bar{c}} = \mathbf{r}^T \mathbf{C}_{\tilde{\mathbf{x}}} \mathbf{r}, \tag{2}$$

where $\mathbf{C}_{\tilde{\mathbf{x}}}$ is the solution covariance. Thus it is necessary to determine the uncertainty of the three-dimensional tracer distribution in order to calculate the uncertainty of the global mean.

4.2. Sources of uncertainty

The uncertainty is determined by the three types of constraints that define the state estimation problem: 1) prior information about the tracer distribution and circulation, 2) proxy observations, and 3) the kinematic tracer conservation model. These constraints relate the tracer distribution and circulation, and thus an uncertainty in one will affect the other. Constraint 1) is some prior knowledge of the state: $\mathbf{x} = \mathbf{x}_0 + \mathbf{u}$, where $\mathbf{x}_0$ is a first guess of the state vector and $\mathbf{u}$ is the deviation from the first guess. Constraint 2) is a collection of observational equations: $\mathbf{y} = \mathbf{E}\mathbf{x} + \mathbf{n}$, where $\mathbf{y}$ is a vector of observations, $\mathbf{E}$ predicts the observations from the state, and $\mathbf{n}$ is the observational error. Constraint 3) is the statistically steady-state conservation equation that, when discretized, becomes $\mathcal{L}[\mathbf{x}] = \mathbf{q} + \mathbf{v}$, where $\mathcal{L}$ is a nonlinear operator due to the multiplication of the tracer concentration and flow field that encapsulates advective and diffusive processes, and $\mathbf{v}$ is the source deviation from the first-guess, $\mathbf{q}$. The model equation includes surface concentration (i.e., Dirichlet) boundary conditions. In this general state estimation framework, the solution state is determined by minimizing a cost function that combines the constraints, $J = \mathbf{u}^T\mathbf{S}^{-1}\mathbf{u} + \mathbf{n}^T\mathbf{W}^{-1}\mathbf{n} + \mathbf{v}^T\mathbf{Q}^{-1}\mathbf{v}$, where $\mathbf{S}, \mathbf{W}$, and $\mathbf{Q}$ are matrices that provide the relative weightings.

Under the assumption that this cost function adequately represents the dominant constraints, all information for an uncertainty analysis in the neighborhood of the known solution is available. The squared standard error, or dispersion of $\tilde{\tilde{c}} - <\tilde{\tilde{c}}>$, is (following Appendix A)

$$\mathbf{C}_{\tilde{\mathbf{x}}} = (\mathbf{S}^{-1} + \mathbf{E}^T\mathbf{W}^{-1}\mathbf{E} + \mathbf{L}_{\tilde{\mathbf{x}}}^T\mathbf{Q}^{-1}\mathbf{L}_{\tilde{\mathbf{x}}})^{-1}, \tag{3}$$

where $\mathbf{L}_{\tilde{\mathbf{x}}}$ is the model linearized about the state, $\tilde{\mathbf{x}}$ (i.e., $\mathbf{L}_{\tilde{\mathbf{x}}} \equiv \partial\mathcal{L}/\partial\mathbf{x}]_{\tilde{\mathbf{x}}}$). Equation (3) assumes that the weight matrices are chosen to be the expected second-

moment matrices of the residuals (i.e., $\mathbf{R}_{nn} = \mathbf{W}$, $\mathbf{R}_{qq} = \mathbf{Q}$, and $\mathbf{R}_{xx} = \mathbf{S}$, following Wunsch (1996)), which has been done in this work, and also assumes that the linear problem is a good surrogate for the more complete nonlinear method.

Substitution of equation (3) into (2) permits the global-mean uncertainty to be written explicitly in terms of the known input variables in the problem:

$$\mathbf{C}_{\bar{c}} = \mathbf{r}^T (\mathbf{S}^{-1} + \mathbf{E}^T \mathbf{W}^{-1} \mathbf{E} + \mathbf{L}_{\tilde{\mathbf{x}}}^T \mathbf{Q}^{-1} \mathbf{L}_{\tilde{\mathbf{x}}})^{-1} \mathbf{r}. \tag{4}$$

Equation (4) illustrates that the three contributions to the uncertainty come from the three constraints: the first-guess uncertainty in the state ($\mathbf{S}^{-1}$), the uncertainty related to the observations ($\mathbf{E}^T \mathbf{W}^{-1} \mathbf{E}$), and the uncertainty related to the imperfect model ($\mathbf{L}_{\tilde{\mathbf{x}}}^T \mathbf{Q}^{-1} \mathbf{L}_{\tilde{\mathbf{x}}}$). While these three terms have clear contributions to the uncertainty, they are under the inverse in the equation and thus the total uncertainty is not simply a linear combination of the three parts.

5. Uncertainty in glacial-mean δ^{13}C

The glacial-mean δ^{13}C and its uncertainty are calculated by adapting equation (4) for $\delta^{13}C_{DIC}$. The input variables include the weighting matrices for the different constraints, taken here as simplified versions from the state estimate. The $\mathbf{S}^{-1}$ matrix is chosen to reflect prior knowledge of the $\delta^{13}C_{DIC}$ field and circulation. For example, the surface $\delta^{13}C_{DIC}$ is assumed to vary by no more than 2.4‰ with lengthscales no smaller than 10° of latitude or longitude. The mass flux ratios, $\mathbf{m}$, are given a prior uncertainty of 0.3 (relative to their nondimensional range of 0 to 1), chosen by the standard deviation of the $\mathbf{m}$ entries for the modern-day circulation. This choice reflects our desire to constrain the glacial circulation with little subjective prior information, but to require that the statistics of

glacial transport should not fall outside the range of the modern-day statistics. For the modern-day circulation, on the other hand, we estimate that the uncertainty of the m values is about 0.05, based on the differences between various modern solutions. The $\mathbf{W}^{-1}$ matrix assumes that the observational uncertainty is 0.2‰, derived from the standard deviation of the misfit between Holocene core values and the reconstructed modern-day seawater properties. (Systematic errors in this relationship will be addressed in Section 6.4.) The choice of the $\mathbf{Q}^{-1}$ matrix conservatively assumes that the glacial source of remineralized material is the same magnitude as the modern day source or sink. The full solution uncertainty (equation 3) is never needed explicitly, thus avoiding the storage of a 1.8 TB matrix (the state has 475773 elements and $\mathbf{C}_{\tilde{\mathbf{x}}}$ has this dimension squared). As $\mathbf{r}$ is a column vector, we can break equation (4) into two parts, one a matrix-vector product and one a vector inner product, such that memory usage is minimized.

Adding the uncertainty estimate to the glacial-mean calculated in Section 3, we find that the LGM mean $\delta^{13}C_{DIC}$ is $\overline{\delta^{13}C_{DIC}}^{G} = 0.14‰ \pm 0.20‰$ and the reference modern-day estimate is $\overline{\delta^{13}C_{DIC}}^{M} = 0.47‰ \pm 0.03‰$. Under the assumption that the LGM and modern estimates are independent, the LGM-to-modern difference is $\Delta_{MG}[\overline{\delta^{13}C_{DIC}}] = 0.32‰ \pm 0.20‰$ (after rounding). Our estimate provides corroborating evidence for both 1) a recent data-based estimate of $0.34‰ \pm 0.19‰$ (Peterson et al., 2014) and 2) a forward circulation model that reproduced about 100 observations and found a change of $\Delta_{MG}[\overline{\delta^{13}C_{DIC}}] = 0.31‰ \pm 0.20‰$ (Tagliabue et al., 2009).

5.1. Observational sensitivity

Obvious candidates to contribute to the uncertainty include the sparsity, measurement error, and representativeness of the observations. Here we address how

the number of sediment core observations affects the resulting uncertainty. We test a range of 10 to 15000 sediment core observations. For the hypothetical cases where we have fewer observations than actually observed, we randomly "observe" a subset of the true observations. This constraint is symbolically written: $\breve{\mathbf{y}} = \breve{\mathbf{E}}\mathbf{x} + \breve{\mathbf{n}}$, where the variables with the breve mark have rows deleted from the original $\mathbf{E}$ definition. The actual observational values do not matter in this calculation, but only that the observational term ($\mathbf{E}$ in the second term on the right hand side of equation 4) is modified. We report the mean of the five experimental trials. For hypothetical cases with more observations than reality, we augment the actual observations with additional observations taken randomly from the seafloor, although this is not entirely realistic due to issues with carbonate preservation, species habitats, and sediment availability. Again we perform five trials with the modified $\breve{\mathbf{E}}$ matrix to help make the statistics more robust.

The uncertainty decreases with an increasing number of observations according to an apparent power law (e.g., $\sigma_{\bar{c}} \approx 2‰/\sqrt{N}$), where N is the number of observations (Figure 3). This function is consistent with the uncertainty estimate for the actual number of observations ($2\sigma_{\bar{c}} = 0.20‰$ for $N = 492$, not plotted). Between $N = 500$ and $N = 1000$, the slope of the power law increases, suggesting that the additional randomly-distributed data points sample the ocean better than the irregularly-clustered 492 data points that are actually available, and indicating that a strategic sampling plan (e.g., see Section 6.1) would produce an even greater reduction in uncertainty. Limitations on the presence of *Cibicidoides* calcite on the seafloor would also provide a constraint for a sampling strategy. In tests where the number of observations is increased past 15000, the standard error does not decrease below $0.06‰$, suggesting that seafloor observations are eventu-

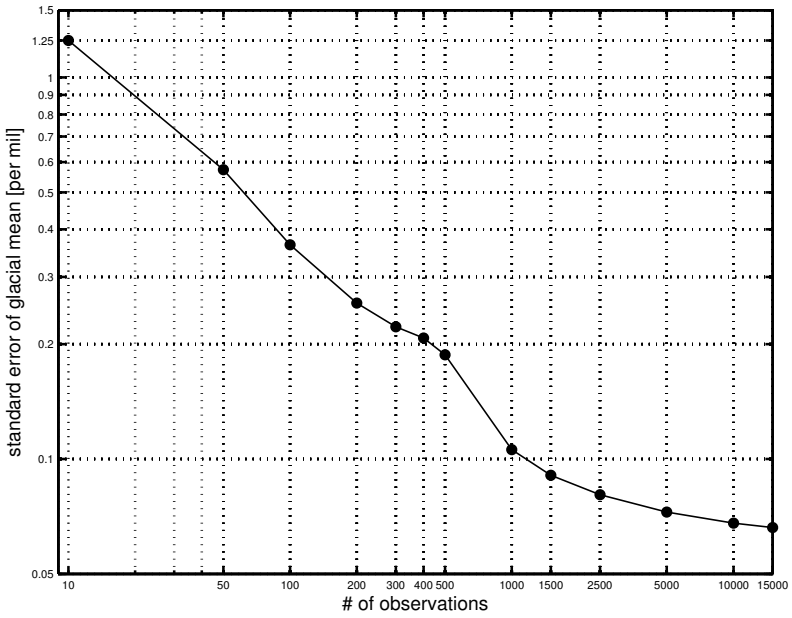

Figure 3: The standard error ($2\sigma_{\bar{c}}$) of the glacial-mean $\delta^{13}C_{DIC}$ as a function of number of observations, on a log-log set of axes. Each circle represents the average of five trials. For $N = 10$ to $N = 400$, a subset of actual observational locations is used. For $N = 500$ to 15000, the 492 actual observations are augmented with observations randomly distributed along the lateral and bottom oceanic boundaries.

ally limited in their ability to record interior ocean signals, and only non-seafloor observations could help at that point.

5.2. Circulation dependence

A second major contributor to uncertainty is the circulation field. In this steady-state scenario, the mass fluxes are expressed as dimensionless mass flux ratios, **m**, that are bounded by 0 and 1 (recall the discussion of the model in Section 2). Here we calculate the sensitivity of the standard error of the global mean $\delta^{13}C_{DIC}$ to the assumed uncertainty in the circulation, as calculated by keeping

all input variables constant in equation (4) but adjusting the part of the $\mathbf{S}^{-1}$ matrix corresponding to the circulation. For cases where the circulation is known as well or better than the modern-day ($\sigma_m < 0.05$), the resulting global mean uncertainty cannot be reduced below 0.03‰ due to the observational characteristics (Figure 4). This limit is lower than previously estimated (e.g., 0.26‰, Ciais et al., 2012), which we interpret as being a result of the improved reconstruction ability of the state estimate. For circulation uncertainties greater than 0.05, the standard error increases rapidly from 0.05‰ to 0.6‰ with increasing circulation uncertainty, and follows an approximate exponential relation (i.e., $\sigma_{\bar{c}} \approx 0.3‰\sigma_m^{0.8}$). The prior estimate of circulation uncertainty, σ_m, is a difficult quantity to estimate, and our assumed glacial uncertainty of 0.3 is in the middle of the sensitive range. This sensitive dependence is because the circulation is used to interpolate data points over far-flung regions of the globe.

5.3. Regional analysis

A more traditional means of analysis is to break the ocean into subdomains to quantify the geographic contribution to global-mean uncertainty. Here, regional means are calculated by taking subdomains of the global domain and recalculating the mass-weighting vector, $\mathbf{r}$, in equation (4). Specifically, the elements of $\mathbf{r}$ that correspond to locations outside the region of interest are set to zero, and the vector is renormalized such that the elements sum to one. Here we select 13 regions of interest in an attempt to compare to the recent work of Peterson et al. (2014).

The primary geographic contributors to global-mean uncertainty are the Surface and North Atlantic regions ($\sigma_{\bar{c}} > 0.6‰$ in Table 1). This result does not straightforwardly proceed from a consideration of the number of observations in any given region. For example, both the Surface and Deep regions have less than

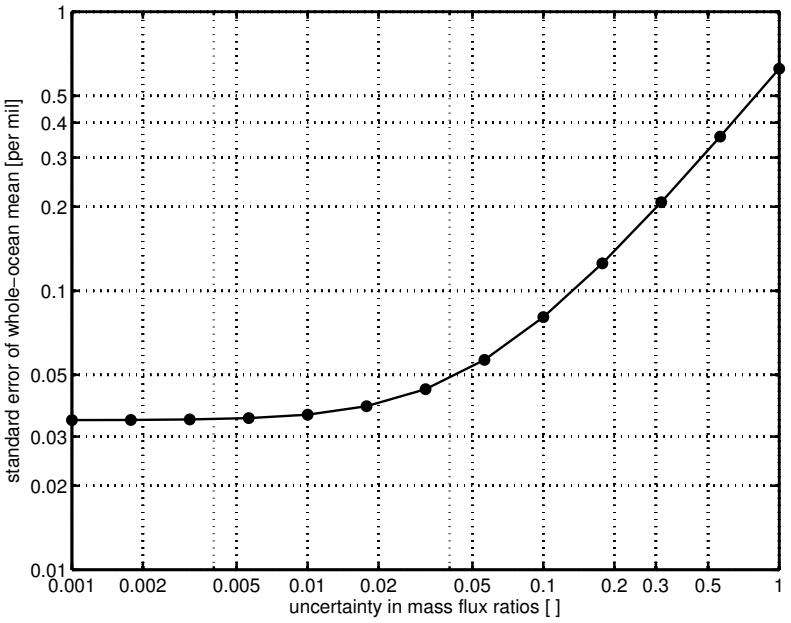

Figure 4: Same as Figure 3, but the standard error ($2\sigma_{\bar{c}}$) of the glacial-mean $\delta^{13}C_{DIC}$ as a function of how well the circulation (in terms of nondimensional mass-flux ratios) is known. An uncertainty of $\sigma_m = 1$ in the mass-flux ratios represents zero circulation knowledge. The modern-day circulation uncertainty is estimated to be $\sigma_m = 0.05$.

Region	$\Delta_{MG}[\overline{\delta^{13}C_{DIC}}]$	$\overline{\delta^{13}C_{DIC}}^{M}$	N_M	μ_M	σ_M	$\overline{\delta^{13}C_{DIC}}^{G}$	N_G	μ_G	σ_G
Global	0.32 ± 0.20	0.46 ± 0.03	19922	0.09	0.28	0.15 ± 0.19	492	0.01	0.19
Deep	0.49 ± 0.23	0.37 ± 0.02	229	0.05	0.21	-0.12 ± 0.22	0	-	-
Surface	0.06 ± 0.70	1.06 ± 0.07	8453	0.21	0.36	1.01 ± 0.70	6	-0.01	0.05
NW Atlantic	0.16 ± 0.67	0.96 ± 0.06	321	0.11	0.20	0.80 ± 0.67	72	-0.02	0.18
NE Atlantic	0.25 ± 0.85	0.99 ± 0.25	540	0.10	0.15	0.74 ± 0.81	155	0.01	0.22
SW Atlantic	0.41 ± 0.31	0.77 ± 0.02	836	-0.03	0.14	0.36 ± 0.31	45	0.06	0.23
SE Atlantic	0.60 ± 0.21	0.72 ± 0.05	274	0.00	0.13	0.12 ± 0.20	79	0.04	0.23
South Atlantic	0.84 ± 0.40	0.62 ± 0.06	23	0.21	0.20	-0.22 ± 0.40	23	0.02	0.27
North Pacific	0.13 ± 0.27	-0.08 ± 0.02	1254	0.03	0.22	-0.21 ± 0.27	65	-0.01	0.11
South Pacific	0.33 ± 0.33	0.35 ± 0.01	4157	0.00	0.15	0.02 ± 0.33	36	0.00	0.08
Indian	0.25 ± 0.32	0.34 ± 0.01	2735	-0.04	0.12	0.09 ± 0.32	42	0.02	0.12
Southern (AI)	1.22 ± 0.85	0.54 ± 0.03	648	0.06	0.10	-0.68 ± 0.85	0	-	-
Southern (P)	0.44 ± 0.30	0.45 ± 0.02	401	0.01	0.10	0.01 ± 0.30	1	0.07	-

Table 1: Mean $\delta^{13}C_{DIC}$ with error estimates and statistics for 13 oceanic regions defined by Peterson et al. (2014). The quantities include (*from left column to right*): global-mean LGM-to-modern $\delta^{13}C$ change and 2-σ uncertainty ($\Delta_{MG}[\overline{\delta^{13}C_{DIC}}]$), modern-day mean $\delta^{13}C_{DIC}$ and 2σ uncertainty ($\overline{\delta^{13}C_{DIC}}^{M}$), number of modern-day observations (N_M), mean modern-day model-data misfit (μ_M), standard deviation of modern-day model-data misfit (σ_M), LGM mean $\delta^{13}C_{DIC}$ and 2σ uncertainty ($\overline{\delta^{13}C_{DIC}}^{G}$), number of LGM observations (N_G), mean LGM model-data misfit (μ_G), and standard deviation of LGM model-data misfit (σ_G). Three large-scale regions are included: Global, Deep (everywhere below 5 km depth), and Surface (everywhere shallower than 500 m). The Atlantic is split into five regions: NW (west of 33°W, north of 0°), NE (east of 33°W, north of 0°), SW (west of 15°W, 0° to 55°S), SE (east of 15°W, 0° to 55°S), and South Atlantic (east of 22°W, 40°S to 55°S). The Pacific is split into two regions: North Pacific (0° to 60°N) and South Pacific (0° to 66°S). The Indian Ocean is defined as one region (north of 55°S, 30°E to 125°E). The Southern Ocean is split into two parts: Atlantic-Indian (AI) sector (south of 55°S) and the Pacific (P) sector (south of 66°S). See Figure 1 of Peterson et al. (2014) for complete boundaries.

10 observations, yet the Deep region has much more moderate uncertainty (0.23‰ versus 0.70‰ in the Surface). Waters that enter the Deep region must pass through observations at shallower depths, and are therefore somewhat constrained by the numerical model and observations. The uncertainty in the North Atlantic occurs despite over 200 LGM observations in those regions, and results from the nearly-unobserved $\delta^{13}C_{DIC}$ values in the Nordic, Mediterranean, and Caribbean Seas. The center of the North Atlantic, on the other hand, has some of the lowest estimated errors, but this is masked by our choice of regional boundaries.

The model fits the observations to an acceptable level in almost all regions, as evidenced by the standard deviation of the modern and glacial model-data misfits, σ_M and σ_G, being less than or equal to 0.2‰. One exception is the modern-day surface ($\sigma_M = 0.36$‰) which may be symptomatic of seasonal variations not captured by the steady-state model. The model-data misfit also has a strong mean offset in the modern-day surface ocean ($\mu_M = 0.21$‰), that results from the filtering of the Suess effect in the surface ocean and leads to the state estimate having more positive $\delta^{13}C_{DIC}$ than the contaminated observations. Even over the entire globe, the modern-day state estimate is on average 0.09‰ more enriched in $\delta^{13}C_{DIC}$ than the observations, roughly consistent with a forward model (Tagliabue and Bopp, 2008) that found a pre-industrial-to-modern change of 0.12‰ when constrained by observations (Gruber et al., 1999). Here, the accounting for the Suess effect makes a 1σ (equal to one standard error) shift in the estimated LGM-to-modern global-mean $\delta^{13}C_{DIC}$ change.

Up to this point, we have emphasized the agreement of our global-mean estimate with previous studies, and generally speaking, our regional results are also consistent with previous regional estimates (e.g., Oliver et al., 2010; Peterson

et al., 2014). In a detailed investigation of the Deep (> 5km) region, however, our model reconstructs a 0.49‰ change, suggesting that the 0.74‰ estimate of Peterson et al. (2014) is an overestimate owing to the extrapolation by their assumed linearly-varying vertical structure. In the Surface region, there are similarities in the estimates (here: $\Delta_{MG}[\overline{\delta^{13}C_{DIC}}] = 0.07‰ \pm 0.71‰$, Peterson et al. (2014): $0.02‰ \pm 0.40‰$), but here we use a more sophisticated reconstruction technique yet obtain larger uncertainties, suggesting that their ad-hoc error bar is an underestimate. Our large Surface region error bars indicate that the best place to isolate a reservoir from benthic foraminiferal detection is not the bottom ocean, but instead the upper thermocline waters that primarily recirculate in the subtropics and tropics. This result points toward the need to compile planktonic $\delta^{13}C_{DIC}$ records (e.g., Broecker and McGee, 2013) such that they can be used in concert with benthic records. In this regard we note that there is convincing evidence indicating the $\delta^{13}C$ of planktonic foraminifera shells vary with seawater carbonate ion concentration (Spero et al., 1997; Russell and Spero, 2000; Peeters et al., 2002). Although this effect has not been identified in benthic foraminifera, its pervasive presence among many species of planktonic foraminifera suggests that deep water carbonate ion variations between the modern and glacial could shift benthic foraminifera shell $\delta^{13}C$ away from a 1:1 relationship with $\delta^{13}C_{DIC}$ and contribute to uncertainties in these modeled reconstructions (see Section 6.4).

6. Discussion

6.1. Large $\delta^{13}C$ change scenario

The LGM-to-modern $\delta^{13}C_{DIC}$ change presented in Section 3 falls at the low end of the spectrum of previous marine-based estimates, and is very low when

compared to terrestrial-based carbon reservoir inferences (e.g., Crowley, 1995). The state estimation method reverts to the modern-day circulation in the absence of any paleo-data. Thus, the $\Delta_{\mathrm{MG}}[\overline{\delta^{13}\mathrm{C}_{\mathrm{DIC}}}]$ estimate could be biased low because of remnant modern-day constraints pulling the estimate toward no change. A low estimate may also be due to low temporal resolution in the cores, as suggested by a selection of high-resolution cores that indicates $\Delta_{\mathrm{MG}}[\overline{\delta^{13}\mathrm{C}_{\mathrm{DIC}}}]$ may be as high as 0.6‰ (A. Mix, personal communication, 2014). Such a high estimate would then bring the marine and terrestrial estimates closer to consistency. Here we have attempted to account for the resolution issue by removing cores using an δ^{18}O criterion (discussed in Section 2.2), but we believe it is worth addressing these issues in greater detail by performing a test to determine whether a large $\Delta_{\mathrm{MG}}[\overline{\delta^{13}\mathrm{C}_{\mathrm{DIC}}}]$ is consistent with the observations and a steady-state circulation. To perform this test, we add an additional "observation" that the LGM-mean $\delta^{13}\mathrm{C}_{\mathrm{DIC}}$ is 0.6‰ less than the modern-day with a small uncertainty of 0.01‰. As in Section 5.1, this modification is handled by introducing a modified observational matrix, vector, and weighting: $\check{\mathbf{E}}$, $\check{\mathbf{y}}$, and $\check{\mathbf{W}}$. The nonlinear solution method of Section 2 is then run with these additions and no other changes.

A second LGM state estimate (hereafter, LGM State Estimate 2) is indeed capable of fitting the data while producing a whole-ocean change of $\Delta_{\mathrm{MG}}[\overline{\delta^{13}\mathrm{C}_{\mathrm{DIC}}}]=$ 0.59‰ (Figure 5). The spatial pattern of remaining model-data misfits do not suggest that the phytodetritus or carbonate ion effect are at play. The circulation pattern leads to a deep (greater than 3km) northern-southern water-mass interface in the Atlantic Ocean, similar to that in LGM estimate 1. The standard deviation of the model-data misfit is actually smaller than that for LGM estimate 1 (LGM 1: $\sigma_G = 0.19$‰, LGM 2:$\sigma_G = 0.17$‰). LGM state estimate 2, however,

is barely capable of fitting the data without introducing a significant mean offset. The estimated mean model-data misfit of $\mu_G = -0.03‰$ is insignificant at the 5% level, but just so ($p = 0.06$ for $N = 492$). The larger whole-ocean change is due to increased changes in specific regions, such as the Atlantic sector of the Southern Ocean where $\Delta_{MG}[\delta^{13}C_{DIC}] > 1.4‰$. The zonally-averaged $\Delta_{MG}[\delta^{13}C_{DIC}]$ in the core of North Pacific Intermediate Water increases from $-0.1‰$ to $0.5‰$ as well, indicating that the observations located along the margins are not sufficient to constrain the Pacific zonal mean. In addition, the unconstrained Arctic Ocean has much increased $\Delta_{MG}[\delta^{13}C_{DIC}]$ at intermediate levels.

The difference in $\delta^{13}C_{DIC}$ between the two LGM state estimates, $\Delta_{GG}[\delta^{13}C_{DIC}]$ (the difference of two glacial "G" estimates), can be thought of as the observational null space and illustrates the ocean regions that are both unconstrained and important for setting the global mean. The biggest differences occur at the sea surface and the Southern Ocean (Figure 6). Increased $\Delta_{GG}[\delta^{13}C_{DIC}]$ in the Atlantic sector of the Southern Ocean also requires an increased $\Delta_{GG}[\delta^{13}C_{DIC}]$ in the inflow of this water into the Pacific Ocean due to the circulation constraints. Surface differences, especially in the Pacific Ocean, are as large as $1‰$, and are consistent with the large error bars previously detailed in Table 1. Should the planktonic $\delta^{13}C$ records that indicate little change between the LGM and modern-day (e.g., Broecker and McGee, 2013) be representative of the entire tropics, LGM state estimate 1 (from Sections 3-5) would be considered more reasonable. Our map of the difference between the two LGM state estimates emphasizes the regions in which additional observations would be most useful.

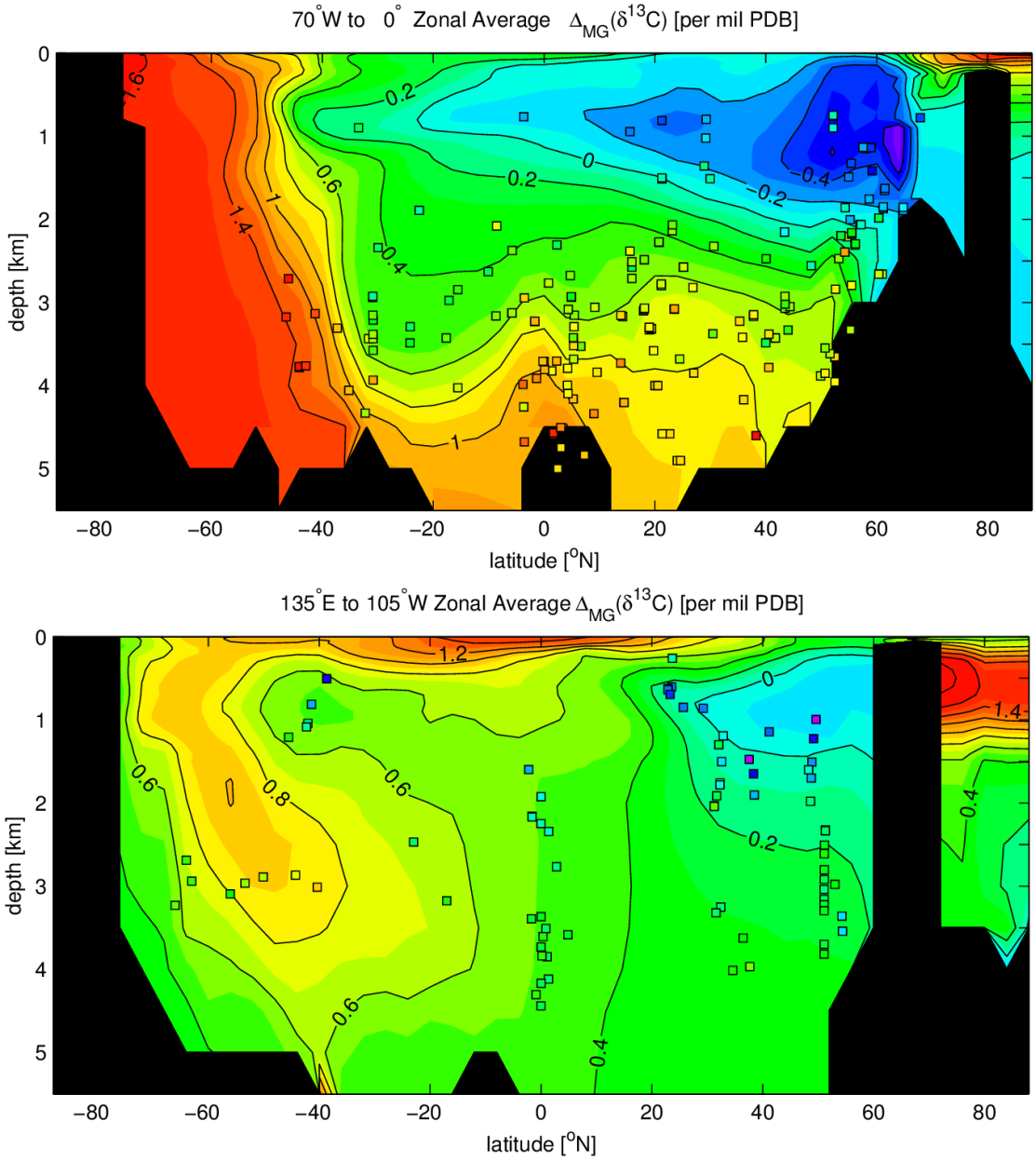

Figure 5: Atlantic and Pacific zonal-average difference of $\delta^{13}C$ between LGM estimate 2 and modern-day (i.e., $\Delta_{MG}[\delta^{13}C_{DIC}] = \delta^{13}C^{M}_{DIC}$ - $\delta^{13}C^{G2}_{DIC}$).

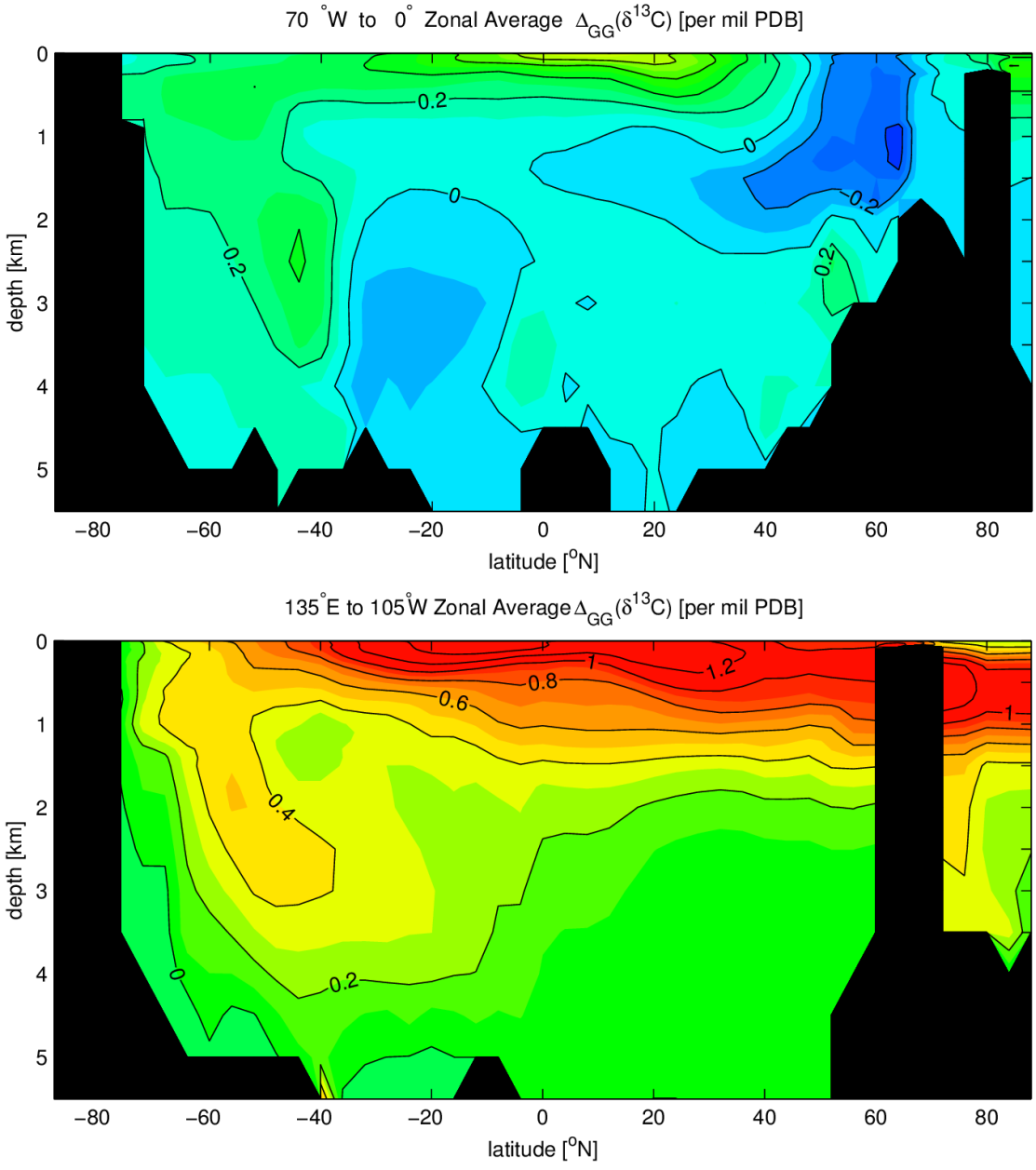

Figure 6: Atlantic and Pacific zonal-average difference of $\delta^{13}C_{DIC}$ between 2 LGM Estimates ($\Delta_{GG}[\delta^{13}C_{DIC}] = \delta^{13}C^{G2}_{DIC}$ - $\delta^{13}C^{G}_{DIC}$).

6.2. *Optimal data weights*

Given a circulation field, the state estimate formulation permits the optimal set of data weights in equation (1) to be explicitly calculated (following Appendix B)

$$\mathbf{w} = \mathbf{W}^{-1}\hat{\mathbf{E}}(\hat{\mathbf{S}}^{-1} + \hat{\mathbf{E}}^T\mathbf{W}^{-1}\hat{\mathbf{E}} + \mathbf{L}_\mathbf{c}^T\mathbf{Q}^{-1}\mathbf{L}_\mathbf{c})^{-1}\hat{\mathbf{r}}, \tag{5}$$

where the hat represents truncating the variables to the quantities related to the tracer field. Interestingly, the elements of $\mathbf{w}$ need not sum to one, nor are they necessarily non-negative. The additional, usually-neglected constant in equation (1) is

$$\bar{c}_0 = (\mathbf{c}_0^T\hat{\mathbf{S}}^{-1} + \mathbf{q}^T\mathbf{Q}^{-1}\mathbf{L}_\mathbf{c})(\hat{\mathbf{S}}^{-1} + \hat{\mathbf{E}}^T\mathbf{W}^{-1}\hat{\mathbf{E}} + \mathbf{L}_\mathbf{c}^T\mathbf{Q}^{-1}\mathbf{L}_\mathbf{c})^{-1}\hat{\mathbf{r}}, \tag{6}$$

and it is related the sampling bias. If all the observations have a value of zero, the best estimate of the global mean has a value of $\bar{c}_0$, indicating that prior information is being used to calculate the global mean. Thus, the degree to which the observations sample the global ocean in a biased way is quantified. In the case that no observations are available, $\bar{c}_0$ reverts to the first-guess global mean.

The map of observational weights is spatially heterogeneous with Eastern Atlantic points generally having the smallest weights (Figure 7). A point in the Indian Ocean is upweighted the most, with $w \approx 10/N$ (or 10 times the weight that it would be given in the basic arithmetic mean). This map generally corresponds to the upweighting of Pacific data points (due to their relative sparsity) and downweighting of Atlantic points. Finer detail is also present, however, such as the upweighting of the few points in the Nordic Seas, but a downweighting of nearby points that are just south of the Greenland-Iceland-Scotland ridge. Other details depend on the flow patterns in the glacial circulation, as observations have influence both up- and downstream.

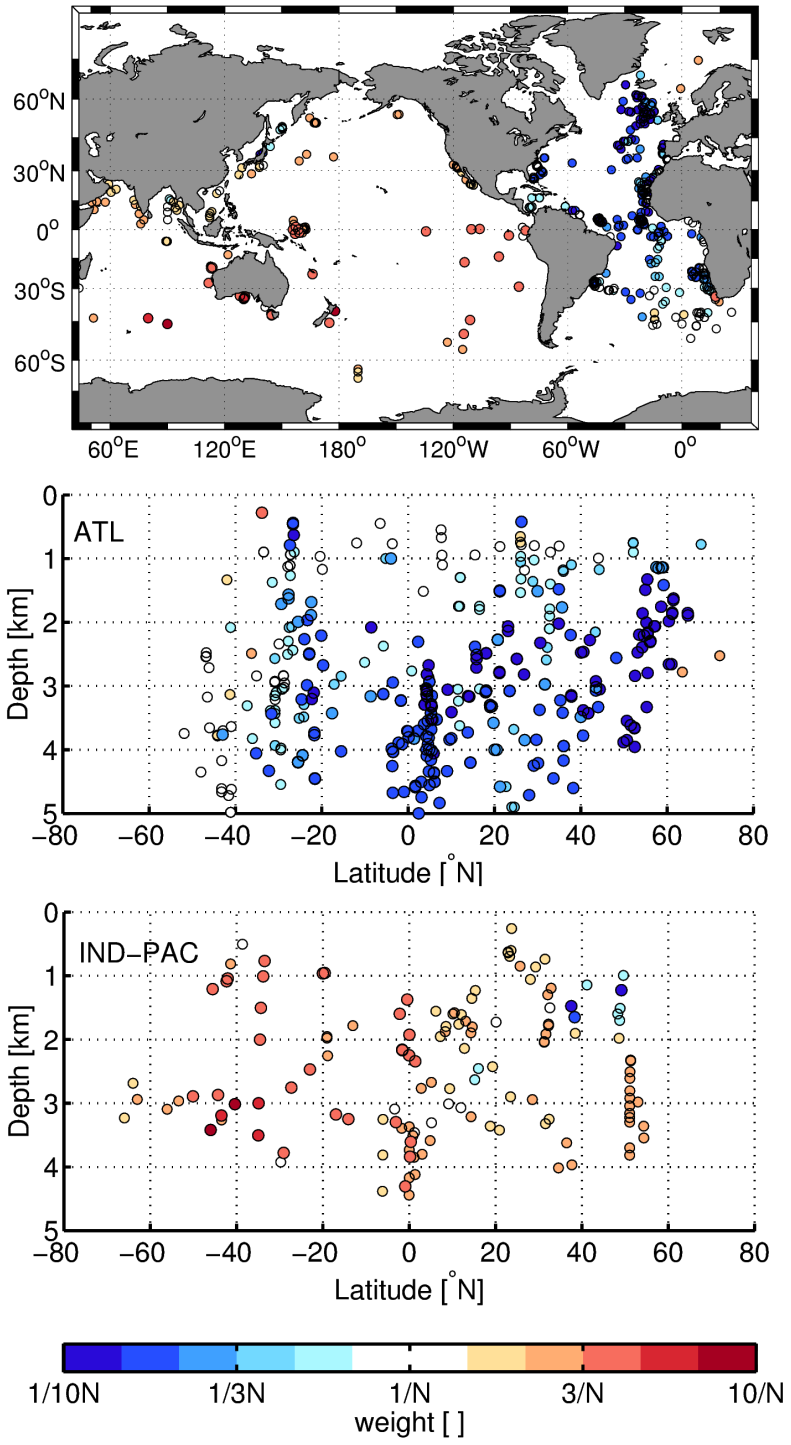

Figure 7: Optimal observational weights to construct a global mean given the glacial circulation (LGM State Estimate 1): plan view (*top*), Atlantic data (*middle*) and Indo-Pacific data (*bottom*). The colorscale is logarithmic. The weights vary from 10 times greater to 100 times lesser than the arithmetic-mean weight and thus some values are offscale low (saturated at a value of $1/10N$).

6.3. Interpreting data histograms

Important information about $\Delta_{\mathrm{MG}}[\overline{\delta^{13}\mathrm{C}_{\mathrm{DIC}}}]$ is available by aggregating pointwise estimates of $\Delta_{\mathrm{MG}}[\delta^{13}\mathrm{C}_{\mathrm{DIC}}]$ in a histogram. Pointwise values of $\Delta_{\mathrm{MG}}[\delta^{13}\mathrm{C}_{\mathrm{DIC}}]$ are here inferred by projecting the modern-day state estimate $\delta^{13}\mathrm{C}_{\mathrm{DIC}}$ field onto the core sites by a linear interpolation of the 8 nearest gridpoints, then comparing with LGM sediment core values. In our 492 points of $\Delta_{\mathrm{MG}}[\delta^{13}\mathrm{C}_{\mathrm{DIC}}]$, the median is 0.45‰ and the mean is 0.39‰ (upper left panel Figure 8). The mode of the distribution is 0.6‰, which may explain why Shackleton (1977) was more likely to estimate a number this high with a small number of cores. It is not clear from this analysis, however, whether the mean of the histogram is a good estimate for the global-mean $\delta^{13}\mathrm{C}_{\mathrm{DIC}}$.

To better interpret such a histogram, consider formulating a modern-day and LGM equation of the type of equation (1) and taking their difference. For a general tracer, we obtain

$$\Delta_{\mathrm{MG}}(\overline{c}) = \overline{\overline{\mathbf{w}}}^{T}\Delta_{\mathrm{MG}}(\mathbf{y}) + \Delta_{\mathrm{MG}}(\mathbf{w})^{T}\overline{\overline{\mathbf{y}}} + \Delta_{\mathrm{MG}}(\overline{c}_0), \tag{7}$$

where the Δ_{MG} operator acts elementwise on each vector and the double overbar represents the temporal mean of modern-day and LGM conditions (to distinguish from the single overbar that is a global spatial average). The mean of the aforementioned histogram reflects the true global mean in the case that the data weights are based on the arithmetic mean ($\overline{\overline{w}}_i = 1/N$ for all i) and that the second and third terms of equation (7) vanish. As discussed in the Introduction, the spatially irregular distribution of observations makes these conditions improbable, and thus the mean of the histogram is not necessarily a good estimate of global-mean change.

The interpretation is improved when a circulation is available to compute the optimal weights via equations (5) and (6). For illustration, consider a case where

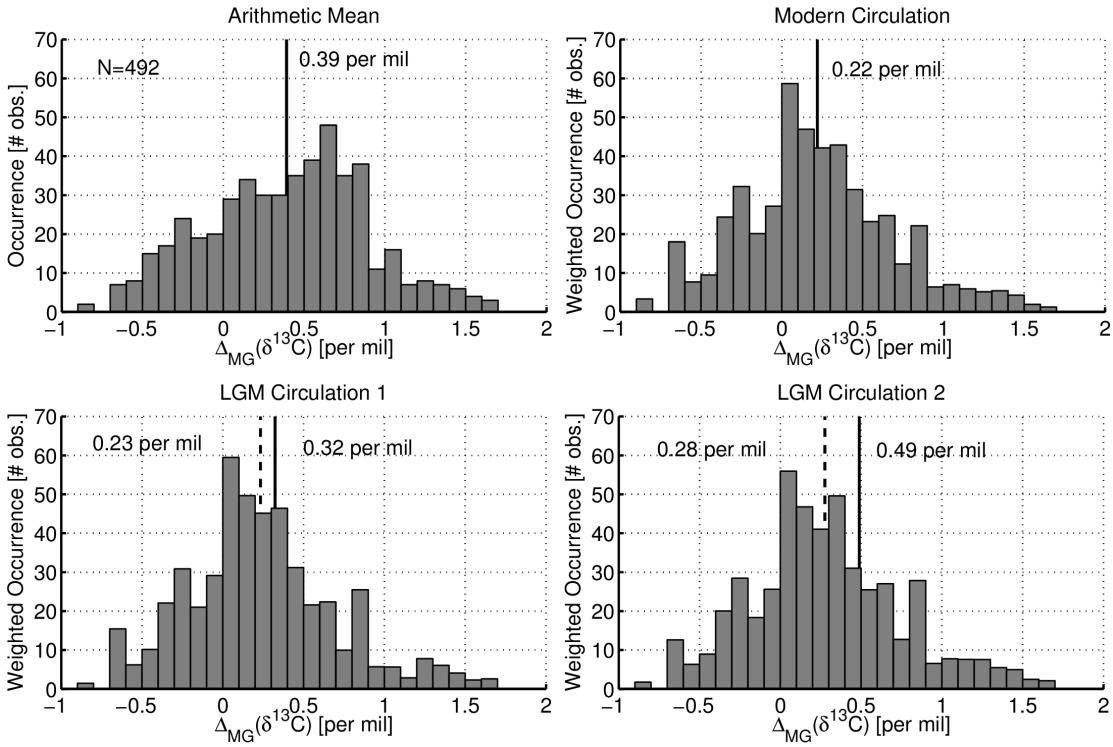

Figure 8: Inference of LGM-to-modern $\delta^{13}C_{DIC}$ change from pointwise measurements. *Upper left*: Histogram of the 492 observations of $\Delta_{MG}[\delta^{13}C_{DIC}]$. *Upper right*: Histogram modified by the optimal weights computed for the modern-day circulation. Histogram modified by the optimal weights computed for the glacial circulation (*lower left*: LGM State Estimate 1, *lower right*: LGM State Estimate 2). The inferred $\Delta_{MG}[\overline{\delta^{13}C_{DIC}}]$ (*solid lines*) results from the mean of the histogram in the top row. In the bottom row, the mean of the histogram (*dashed lines*) is corrected to produce the $\Delta_{MG}[\overline{\delta^{13}C_{DIC}}]$ estimate (*solid lines*).

it is assumed that the modern-day circulation is representative of the LGM. Then we can use the calculated modern-day weights ($\mathbf{w}_M$) to better approximate the first term of equation (7). These weights shift the mode of the distribution to $\Delta_{\mathrm{MG}}[\overline{\delta^{13}\mathrm{C}_{\mathrm{DIC}}}] = 0.05‰$ and the inferred global-mean decreases from 0.39‰ to 0.22‰ (visualized as a weighted histogram, upper right panel, Figure 8). In effect, the observations of smaller change are upweighted because they are located along modern-day circulation pathways that influence more of the ocean.

A full interpretation of the pointwise data should also account for LGM-to-modern circulation change, of course. In particular, we use both the circulations from LGM State Estimate 1 and 2 (lower row, Figure 8). The mean of the histogram is again modified, this time back toward larger values (0.23‰ and 0.28‰, respectively). The two correction terms due to the changing ocean circulation must also be considered (terms 2 and 3 of the right hand side of equation 7). For LGM State Estimate 1, the correction is 0.09‰ and the final estimate of $\Delta_{\mathrm{MG}}[\overline{\delta^{13}\mathrm{C}_{\mathrm{DIC}}}] = 0.32‰$ is consistent with the results showcased in Sections 3 and 5. For LGM State Estimate 2, the correction is even larger: 0.21‰ (dominated by term 3: 0.15‰). Equation (7) then diagnoses a global-mean change of $\Delta_{\mathrm{MG}}[\overline{\delta^{13}\mathrm{C}_{\mathrm{DIC}}}] = 0.49‰$, smaller than the actual 0.59‰, which is symptomatic of the breakdown of the linear assumption (i.e., equation A.4). Unfortunately, the correction terms are poorly known due to the uncertainty in the LGM circulation. We emphasize that the correction cannot be determined from the data histogram alone.

6.4. Carbonate chemistry effects

Here we revisit our definition of $\Delta_{\mathrm{MG}}[\delta^{13}\mathrm{C}_{\mathrm{DIC}}]$ and whether it signficantly differs from $\Delta_{\mathrm{HG}}[\delta^{13}\mathrm{C}_{\mathrm{DIC}}]$, defined as the LGM-to-Late Holocene difference. Infor-

mation regarding $\Delta_{HG}[\delta^{13}C_{DIC}]$ is more directly available through the differencing of LGM and Late Holocene core data. One tradeoff is that only 365 measurements of a Late Holocene and LGM value from the same core are available even when the Late Holocene time interval is extended from 0-6kyr BP. An advantage of this definition is that interlaboratory offsets are irrelevant when using intracore differences. We find that inferring $\Delta_{HG}[\delta^{13}C_{DIC}]$ by this method is not substantially different from our previous $\Delta_{MG}[\delta^{13}C_{DIC}]$ estimate; the median and mean are slightly larger (0.47‰ and 0.43‰, respectively).

A potential hidden error in $\Delta_{HG}[\delta^{13}C_{DIC}]$ estimates, however, could occur due to a systematic error in the $\delta^{13}C$ calcite-to-seawater proxy relationship, for example a dependence of calcite $\delta^{13}C$ on carbonate ion or temperature (e.g., Spero et al., 1997; Hesse et al., 2014). To determine the size of such an effect, we seek an improved calibration between the Late Holocene $\delta^{13}C$ values and the modern-day seawater characteristics including $\delta^{13}C_{DIC}$, temperature, salinity, CO_3^{2-}, DIC, and pH (using MATLAB routines of Zeebe and Wolf-Gladrow, 2001). In this case, we find that the original calcite-seawater calibration can only be marginally improved (standard error: 0.23‰, $r = 0.83$, for the equation: $\delta^{13}C_{DIC} = 1.01\ \delta^{13}C_c - 0.24\ S - 0.024\ T + .0056[CO_3^{2-}] + .0026[DIC] - 0.15[pH] + 3.95$ ($N = 488$). Such a finding suggests that the error due to ignoring these dependencies is smaller than interlaboratory calibration error, although it does not conclusively rule out systematic errors because of the difficulty in reconstructing the appropriate seawater properties at the core sites.

7. Summary

The LGM-to-modern $\delta^{13}C_{DIC}$ change is explicitly estimated by first mapping benthic foraminiferal observations onto a global grid, and then taking a mass-weighted average of the gridded values. The mapping process, however, requires a method more sophisticated than typical interpolation because of the sparsity of the dataset and large spatial gaps. Here we demonstrate that an LGM state estimate derived from a recent compilation of almost 500 $\delta^{13}C$ data points combined with a numerical model can provide a reasonable globally-gridded field, as well as self-consistent uncertainty estimates. Our updated best estimate of LGM-to-modern global $\delta^{13}C_{DIC}$ change is 0.32 ± 0.20‰ at the 2σ uncertainty level. A coherent picture of the LGM $\delta^{13}C$ distribution emerges that is consistent with previous Atlantic estimates and fills in the missing details of the Pacific distribution. Maps of the LGM-to-modern difference in $\delta^{13}C$ also display coherent spatial patterns, with largest changes in the Atlantic sector of the Southern Ocean.

While previous investigators have used various sub-domains and multiple-step averaging techniques to determine how to best weight pointwise observations to obtain the global mean, here we show that determination of the optimal data weights requires knowledge of the ocean circulation. The diagnosed optimal weights conform to expectation in many ways, such as upweighting data in regions with sparse coverage. It is very difficult, however, to determine the global mean change from pointwise histograms of the local $\delta^{13}C_{DIC}$ change unless the concommitant circulation change is also known. Thus, much of the existing uncertainty in LGM-to-modern $\delta^{13}C$ change is due to the difficulty in determining the glacial ocean circulation.

Our glacial state estimate points toward future directions to reduce the consid-

erable remaining global-mean $\delta^{13}C_{DIC}$ uncertainty. For example, the addition of randomly-distributed hypothetical data would reduce the uncertainty of the global mean as $N^{-1/2}$, where N is the number of observations. In addition, we find multiple $\delta^{13}C_{DIC}$ distributions that can fit the data, including one with global mean change of nearly 0.6‰, possibly bringing marine and terrestrial carbon partitioning estimates into consistency. This large $\delta^{13}C$ change scenario has its greatest differences to the best-guess LGM estimate in the upper ocean and Southern Ocean, pointing to regions where additional information can distinguish between these two scenarios. In particular, a compilation of planktonic records would help reduce the uncertainty in surface regions. Provided that challenges with interpretation regarding DIC change and species offsets can be overcome (e.g., Spero et al., 1997), we expect that strategic sampling can reduce the global-mean uncertainty at a faster rate than the hypothetical randomly-sampled case. A two-pronged approach appears best suited to reduce the global-mean uncertainty: compilation of information from strategically-placed locations, including planktonic records, and the implementation of a model with more sophisticated dynamical constraints, especially in the upper ocean.

Appendix A. Uncertainty derivation

Appendix A.1. Least-squares solution

Section 4.2 defines a cost function, $J = \mathbf{u}^T\mathbf{S}^{-1}\mathbf{u} + \mathbf{n}^T\mathbf{W}^{-1}\mathbf{n} + \mathbf{v}^T\mathbf{Q}^{-1}\mathbf{v}$, that is here written in a more complete form by substituting the equations for the first-guess adjustment, the observational constraint, and the model:

$$J = (\mathbf{x}-\mathbf{x}_0)^T\mathbf{S}^{-1}(\mathbf{x}-\mathbf{x}_0) + (\mathbf{E}\mathbf{x}-\mathbf{y})^T\mathbf{W}^{-1}(\mathbf{E}\mathbf{x}-\mathbf{y}) + (\mathcal{L}[\mathbf{x}]-\mathbf{q})^T\mathbf{Q}^{-1}(\mathcal{L}[\mathbf{x}]-\mathbf{q}). \tag{A.1}$$

The solution, $\tilde{\mathbf{x}}$, satisfies the stationary assumption:

$$J_{\tilde{\mathbf{x}}} \equiv \partial J/\partial \mathbf{x}]_{\tilde{\mathbf{x}}} = 2\{\mathbf{S}^{-1}(\mathbf{x}-\mathbf{x}_0)+\mathbf{E}^T\mathbf{W}^{-1}(\mathbf{E}\mathbf{x}-\mathbf{y})+\mathbf{L}_{\tilde{\mathbf{x}}}^T\mathbf{Q}^{-1}(\mathcal{L}[\mathbf{x}]-\mathbf{q})\} = 0. \tag{A.2}$$

We define a linearization of model in the neighborhood of the solution:

$$\mathcal{L}[\mathbf{x}] = \mathcal{L}[\mathbf{x}'] + \mathbf{L}_{\mathbf{x}'}(\mathbf{x}-\mathbf{x}') + \varepsilon, \tag{A.3}$$

where ε represents the higher-order terms in the expansion. The solution estimate, $\tilde{\mathbf{x}}$, satisfies

$$\tilde{\mathbf{x}} = (\mathbf{S}^{-1}+\mathbf{E}^T\mathbf{W}^{-1}\mathbf{E}+\mathbf{L}_{\mathbf{x}'}^T\mathbf{Q}^{-1}\mathbf{L}_{\mathbf{x}'})^{-1}\{\mathbf{S}^{-1}\mathbf{x}_0+\mathbf{E}^T\mathbf{W}^{-1}\mathbf{y}+\mathbf{L}_{\mathbf{x}'}^T\mathbf{Q}^{-1}(\mathbf{q}+\mathbf{L}_{\mathbf{x}'}\mathbf{x}'-\mathcal{L}[\mathbf{x}'])\}, \tag{A.4}$$

where the higher-order terms become negligible as one approaches the solution and are dropped from this last equation.

Appendix A.2. Uncertainty of tracer distribution and circulation

Here we seek the expected solution in the hypothetical case that a perfect first-guess, observations, and tracer source are available ($\mathbf{x}_0^*$, $\mathbf{y}^*$, and $\mathbf{q}^*$, respectively). Defining

$$\mathbf{d}_0 = \mathbf{S}^{-1}\mathbf{x}_0^*+\mathbf{E}^T\mathbf{W}^{-1}\mathbf{y}^*+\mathbf{L}_{\mathbf{x}'}^T\mathbf{Q}^{-1}(\mathbf{q}^*+\mathbf{L}_{\mathbf{x}'}\mathbf{x}'-\mathcal{L}[\mathbf{x}']), \tag{A.5}$$

the expected solution is

$$<\tilde{\mathbf{x}}> = (\mathbf{S}^{-1}+\mathbf{E}^T\mathbf{W}^{-1}\mathbf{E}+\mathbf{L}_{\tilde{\mathbf{x}}}^T\mathbf{Q}^{-1}\mathbf{L}_{\tilde{\mathbf{x}}})^{-1}\mathbf{d}_0. \tag{A.6}$$

The dispersion of $\tilde{\mathbf{x}} - <\tilde{\mathbf{x}}>$ is equal to the solution covariance of $\tilde{\mathbf{x}}$:

$$\mathbf{C}_{\tilde{\mathbf{x}}} \equiv <(\tilde{\mathbf{x}} - <\tilde{\mathbf{x}}>)(\tilde{\mathbf{x}} - <\tilde{\mathbf{x}}>)^T>, \tag{A.7}$$

and substitution of equation (A.6) into (A.7) gives

$$\mathbf{C}_{\tilde{\mathbf{x}}} = (\mathbf{S}^{-1} + \mathbf{E}^T\mathbf{W}^{-1}\mathbf{E} + \mathbf{L}_{\tilde{\mathbf{x}}}^T\mathbf{Q}^{-1}\mathbf{L}_{\tilde{\mathbf{x}}})^{-1} < (\mathbf{d}-\mathbf{d}_0)(\mathbf{d}-\mathbf{d}_0)^T > (\mathbf{S}^{-1} + \mathbf{E}^T\mathbf{W}^{-1}\mathbf{E} + \mathbf{L}_{\tilde{\mathbf{x}}}^T\mathbf{Q}^{-1}\mathbf{L}_{\tilde{\mathbf{x}}})^{-1}. \tag{A.8}$$

Assuming that errors in the first guess, observations, and model are uncorrelated (i.e., $\mathbf{R}_{xn} = 0$, $\mathbf{R}_{xq} = 0$, etc.), the expected value in the right hand side of (A.8) is

$$< (\mathbf{d}-\mathbf{d}_0)(\mathbf{d}-\mathbf{d}_0)^T >= \mathbf{S}^{-1}\mathbf{R}_{xx}\mathbf{S}^{-1} + \mathbf{E}^T\mathbf{W}^{-1}\mathbf{R}_{nn}\mathbf{W}^{-1}\mathbf{E} + \mathbf{L}_{\tilde{\mathbf{x}}}^T\mathbf{Q}^{-1}\mathbf{R}_{qq}\mathbf{Q}^{-1}\mathbf{L}_{\tilde{\mathbf{x}}}. \tag{A.9}$$

Substituting equation (A.9) into (A.8) and assuming that the weight matrices are equal to the expected second-moment matrices of the residuals (i.e., $\mathbf{R}_{nn} = \mathbf{W}$, $\mathbf{R}_{qq} = \mathbf{Q}$, and $\mathbf{R}_{xx} = \mathbf{S}$), we obtain the solution covariance in terms of the known input variables:

$$\mathbf{C}_{\tilde{\mathbf{x}}} = (\mathbf{S}^{-1} + \mathbf{E}^T\mathbf{W}^{-1}\mathbf{E} + \mathbf{L}_{\tilde{\mathbf{x}}}^T\mathbf{Q}^{-1}\mathbf{L}_{\tilde{\mathbf{x}}})^{-1}, \tag{A.10}$$

which is used in the main text as equation (3). The standard error is here defined as $\pm\sqrt{\mathbf{C}_{\tilde{\mathbf{x}}}}$ of the diagonal elements.

Appendix B. Calculation of the optimal observational weights

In the case that the circulation is known exactly, the cost function equation (A.1) can be simplified

$$J = (\mathbf{c}-\mathbf{c}_0)^T\hat{\mathbf{S}}^{-1}(\mathbf{c}-\mathbf{c}_0) + (\hat{\mathbf{E}}\mathbf{c}-\mathbf{y})^T\mathbf{W}^{-1}(\hat{\mathbf{E}}\mathbf{c}-\mathbf{y}) + (\mathbf{L}_\mathbf{c}\mathbf{c}-\mathbf{q})^T\mathbf{Q}^{-1}(\mathbf{L}_\mathbf{c}\mathbf{c}-\mathbf{q}), \tag{B.1}$$

where the hat indicates truncation of the $\mathbf{E}$ and $\mathbf{S}$ matrices to the parts related to the tracer field. Using the least-squares estimate of the tracer solution and the following definition of the global mean, $\bar{c} = \hat{\mathbf{r}}^T\mathbf{c}$, we obtain a simplified equation

$$\tilde{\bar{c}} = \hat{\mathbf{r}}^T(\hat{\mathbf{S}}^{-1} + \hat{\mathbf{E}}^T\mathbf{W}^{-1}\hat{\mathbf{E}} + \mathbf{L}_\mathbf{c}^T\mathbf{Q}^{-1}\mathbf{L}_\mathbf{c})^{-1}(\hat{\mathbf{S}}^{-1}\mathbf{c}_0 + \hat{\mathbf{E}}^T\mathbf{W}^{-1}\mathbf{y} + \mathbf{L}_\mathbf{c}^T\mathbf{Q}^{-1}\mathbf{q}) \tag{B.2}$$

Comparison of the equation (B.2) to equation (1) permits the identification of the optimal data weights:

$$\mathbf{w} = \mathbf{W}^{-1}\hat{\mathbf{E}}(\hat{\mathbf{S}}^{-1} + \hat{\mathbf{E}}^T\mathbf{W}^{-1}\hat{\mathbf{E}} + \mathbf{L}_\mathbf{c}^T\mathbf{Q}^{-1}\mathbf{L}_\mathbf{c})^{-1}\hat{\mathbf{r}}, \tag{B.3}$$

and the additional constant

$$\bar{c}_0 = (\mathbf{c}_0^T\hat{\mathbf{S}}^{-1} + \mathbf{q}^T\mathbf{Q}^{-1}\mathbf{L}_\mathbf{c})(\hat{\mathbf{S}}^{-1} + \hat{\mathbf{E}}^T\mathbf{W}^{-1}\hat{\mathbf{E}} + \mathbf{L}_\mathbf{c}^T\mathbf{Q}^{-1}\mathbf{L}_\mathbf{c})^{-1}\hat{\mathbf{r}}. \tag{B.4}$$

Acknowledgments

The authors thank Ed Boyle, Thomas Chalk, David McGee, and Alan Mix for helpful discussions. GG is supported by NSF grants OIA-1124880 and OCE-1357121, and the WHOI Ocean and Climate Change Institute.

References

Adams, J. M., Faure, H., 1998. A new estimate of changing carbon storage on land since the last glacial maximum, based on global land ecosystem reconstruction. Global and Planetary Change 16, 3–24.

Adkins, J., McIntyre, K., Schrag, D., 2002. The salinity, temperature, and δ^{18}O of the glacial deep ocean. Science 298, 1724–1725.

Boyle, E. A., 1992. Cadmium and δ^{13}C paleochemical ocean distributions during the Stage 2 Glacial Maximum. Annual Review of Earth and Planetary Sciences 20 (1), 245–287.

Bretherton, F., Davis, R., Fandry, C., 1976. A technique for objective analysis and design of oceanographic experiments applied to MODE-73. Deep-Sea Res 23, 559–582.

608 Broecker, W., Maier-Reimer, E., 1992. The influence of air and sea exchange on
609 the carbon isotope distribution in the sea. Global Biogeochemical Cycles 6 (3),
610 315–320.

611 Broecker, W., McGee, D., 2013. The ^{13}C record for atmospheric CO_2: What is it
612 trying to tell us? Earth and Planetary Science Letters 368, 175–182.

613 Ciais, P., Tagliabue, A., Cuntz, M., Bopp, L., Scholze, M., Hoffmann, G., Louran-
614 tou, A., Harrison, S., Prentice, I., Kelley, D., et al., 2012. Large inert carbon
615 pool in the terrestrial biosphere during the Last Glacial Maximum. Nature Geo-
616 science 5 (1), 74–79.

617 Crowley, T. J., 1995. Ice age terrestrial carbon changes revisited. Global Biogeo-
618 chemical Cycles 9 (3), 377–389.

619 Curry, W., Duplessy, J., Labeyrie, L., Shackleton, N., 1988. Changes in the
620 distribution of $\delta^{13}C$ of deep water $\sum CO_2$ between the last glaciation and the
621 Holocene. Paleoceanography 3 (3).

622 Curry, W., Oppo, D., 2005. Glacial water mass geometry and the distribu-
623 tion of $\delta^{13}C$ of $\sum CO_2$ in the Western Atlantic Ocean. Paleoceanography 20,
624 10.1029/2004PA001021.

625 Duplessy, J., Shackleton, N., Fairbanks, R., Labeyrie, L., Oppo, D., Kallel, N.,
626 1988. Deepwater source variations during the last climatic cycle and their im-
627 pact on the global deepwater circulation. Paleoceanography 3 (3).

628 Gebbie, G., 2014. How much did Glacial North Atlantic Water shoal? Paleo-
629 ceanography 29 (3), 190–209.

630 Gebbie, G., Huybers, P., 2010. Total matrix intercomparison: a method for re-
631 solving the geometry of water-mass pathways. J. Phys. Oceanogr. 40 (8), 1710–
632 1728, DOI: 10.1175/2010JPO4272.1.

633 Gruber, N., Keeling, C. D., Bacastow, R. B., Guenther, P. R., Lueker, T. J., Wahlen,
634 M., Meijer, H. A., Mook, W. G., Stocker, T. F., 1999. Spatiotemporal patterns
635 of carbon-13 in the global surface oceans and the oceanic suess effect. Global
636 Biogeochemical Cycles 13 (2), 307–335.

637 Herguera, J., Herbert, T., Kashgarian, M., Charles, C., 2010. Intermediate and
638 deep water mass distribution in the Pacific during the Last Glacial Maximum
639 inferred from oxygen and carbon stable isotopes. Quaternary Science Reviews
640 29 (9), 1228–1245.

641 Hesse, T., Butzin, M., Bickert, T., Lohmann, G., 2011. A model-data compari-
642 son of δ^{13}C in the glacial Atlantic Ocean. Paleoceanography, 26, PA3220. 26,
643 PA3220.

644 Hesse, T., Wolf-Gladrow, D., Lohmann, G., Bijma, J., Mackensen, A., Zeebe,
645 R. E., 2014. Modelling δ^{13}C in benthic foraminifera: Insights from model sen-
646 sitivity experiments. Marine Micropaleontology 112, 50–61.

647 Hide, R., 1969. Dynamics of the atmospheres of the major planets with an ap-
648 pendix on the viscous boundary layer at the rigid bounding surface of an
649 electrically-conducting rotating fluid in the presence of a magnetic field. J. At-
650 mos. Sci. 26, 841–853.

651 IOC, S., 2010. IAPSO: The international thermodynamic equation of seawater–

2010: Calculation and use of thermodynamic properties, intergovernmental oceanographic commission, manuals and guides no. 56.

Kaplan, J. O., Prentice, I. C., Knorr, W., Valdes, P. J., 2002. Modeling the dynamics of terrestrial carbon storage since the last glacial maximum. Geophysical Research Letters 29 (22), 31–1.

Köhler, P., Fischer, H., Schmitt, J., 2010. Atmospheric $\delta^{13}CO_2$ and its relation to pCO_2 and deep ocean $\delta^{13}C$ during the late Pleistocene. Paleoceanography 25 (1).

Mackensen, A., Schumacher, S., Radke, J., Schmidt, D., 2000. Microhabitat preferences and stable carbon isotopes of endobenthic foraminifera: clue to quantitative reconstruction of oceanic new production? Marine Micropaleontology 40 (3), 233–258.

Makou, M. C., Oppo, D. W., Curry, W. B., 2010. South Atlantic intermediate water mass geometry for the last glacial maximum from foraminiferal Cd/Ca. Paleoceanography 25 (4).

Marchal, O., Curry, W., 2008. On the abyssal circulation in the glacial Atlantic. Journal of Physical Oceanography 38 (9), 2014–2037.

Matsumoto, K., Lynch-Stieglitz, J., 1999. Similar glacial and Holocene deep water circulation inferred from Southeast Pacific benthic foraminiferal carbon isotope composition. Paleoceanography 14 (2), 149–163.

Matsumoto, K., Oba, T., Lynch-Stieglitz, J., Yamamoto, H., 2002. Interior hydrog-

raphy and circulation of the glacial pacific ocean. Quaternary science reviews 21 (14-15), 1693–1704.

Nocedal, J., 1980. Updating quasi-Newton matrices with limited storage. Mathematics of computation 35 (151), 773–782.

Oliver, K., Hoogakker, B., Crowhurst, S., Henderson, G., Rickaby, R., Edwards, N., Elderfield, H., 2010. A synthesis of marine sediment core δ 13 c data over the last 150 000 years. Climate of the Past 6, 645–673.

Olsen, A., Abdirahman, O., Bellerby, R., Johannessen, T., Ninnemann, U., Brown, K., Olsson, K., Olafsson, J., Nondal, G., Kivimäe, C., et al., 2006. Magnitude and origin of the anthropogenic CO_2 increase and the ^{13}C Suess Effect in the Nordic Seas since 1981.

Peeters, F. J., Brummer, G.-J. A., Ganssen, G., 2002. The effect of upwelling on the distribution and stable isotope composition of *globigerina bulloides* and *globigerinoides ruber* (planktic foraminifera) in modern surface waters of the NW Arabian Sea. Global and Planetary Change 34 (3), 269–291.

Peterson, C. D., Lisiecki, L. E., Stern, J. V., 2014. Deglacial whole-ocean $\delta^{13}C$ change estimated from 480 benthic foraminiferal records. Paleoceanography.

Russell, A. D., Spero, H. J., 2000. Field examination of the oceanic carbonate ion effect on stable isotopes in planktonic foraminifera. Paleoceanography 15 (1), 43–52.

Schmittner, A., Gruber, N., Mix, A. C., Key, R. M., Tagliabue, A., Westberry, T. K., 2013. Biology and air-sea gas exchange controls on the distribution of

carbon isotope ratios ($\delta^{13}C$) in the ocean. Biogeosciences Discussions 10 (5), 8415–8466.

Shackleton, N., 1977. Carbon 13 in uvigerina: Tropical rainforest history and the equatorial pacific carbonate dissolution cycles. Marine science.

Spero, H. J., Bijma, J., Lea, D. W., Bemis, B. E., 1997. Effect of seawater carbonate concentration on foraminiferal carbon and oxygen isotopes. Nature 390 (6659), 497–500.

Stern, J. V., Lisiecki, L. E., 2014. Termination 1 timing in radiocarbon-dated regional benthic $\delta^{18}O$ stacks. Paleoceanography.

Tagliabue, A., Bopp, L., 2008. Towards understanding global variability in ocean carbon-13. Global Biogeochemical Cycles 22 (1).

Tagliabue, A., Bopp, L., Roche, D., Bouttes, N., Dutay, J., Alkama, R., Kageyama, M., Michel, E., Paillard, D., 2009. Quantifying the roles of ocean circulation and biogeochemistry in governing ocean carbon-13 and atmospheric carbon dioxide at the last glacial maximum. Clim. Past 5, 695–706.

Walker, J. C. G., 1991. Numerical adventures with geochemical cycles. Oxford University Press New York.

Wunsch, C., 1996. The Ocean Circulation Inverse Problem. Cambridge University Press.

Zeebe, R., Wolf-Gladrow, D., 2001. CO_2 in seawater: equilibrium, kinetics, isotopes. Vol. 65 of Elsevier Oceanography Series. Elsevier.